Wear 506-507 (2022) 204440

Contents lists available at ScienceDirect

Wear

journal homepage: www.elsevier.com/locate/wear

An interactive water lubrication mechanism of γ-$LiAlSi_2O_6$ glass-ceramics in friction and wear

Yanan Peng [a,c], Zeyu Wang [a,b,**], Yuantao Fu [c,d], Xiaoqin Zhang [c,d], Jiapeng Chen [a,b,c,d,*]

[a] National Key Laboratory of Science and Technology on Helicopter Transmission, Nanjing University of Aeronautics and Astronautics, Nanjing, 210016, PR China
[b] Department of Information Engineering, Zhengzhou Professional Technical Institute of Electronic & Information, Zhengzhou, 451450, PR China
[c] Research Center for Advanced Micro-/Nano- Fabrication Materials, Shanghai University of Engineering Science, Shanghai, 201620, PR China
[d] Huapu Microelectronic Technology (Ningbo) Co., LTD, Ningbo, 315502, PR China

ARTICLE INFO

Keywords:
γ-$LiAlSi_2O_6$ glass-ceramic
Anti-attrition
Water lubrication

ABSTRACT

Anti-attrition and water lubrication are two areas where ceramics are widely applied. In comparison to pure ceramics, glass-ceramic composite materials are more accessible to machine and manufacture into water lubrication kits. However, current water lubrication theories are mainly applied to ceramic materials such as SiC, Si_3N_4, Al_2O_3 and ZrO_2. Glass-ceramic water lubrication mechanisms are not involved, in particular, the specific development process of low friction glass-ceramics in the water environment is yet unknown, which limits the application of glass-ceramics. As a result, we developed custom-made γ-$LiAlSi_2O_6$ glass-ceramics for a ball and a wafer that were utilized to conduct friction and wear tests. By contrasting the dry and wet friction coefficients between the ball and the wafer, abrasion losses and surface roughnesses of glass-ceramics, particle size distribution and zeta potential of wear debris over time, the water lubrication mechanisms of glass-ceramics in three different friction stages were clarified, the interactive lubrication effects of the electrical double layer and the dynamic fluid pressure ensure that the wet friction coefficient of the glass-ceramics is constant below 0.02.

1. Introduction

Water has progressively replaced oil-based lubricants as sustainable development requirements and environmental protection regulations have improved, owing to its characteristics of environmental protection, high cooling and low viscosity. Under high-speed and light-load scenes, water as a lubricant is mainly used for water pumps, stern tubes and water turbine engine spindles. Under low-speed and heavy-load scenes, it is mainly used for dikes, sluices, hydraulic generator guide vanes and valves, etc. Under low-speed and light-load scenes, it is mainly used for water treatment machinery, conveying equipment, marine rudders, etc. Ceramics had been essential and frequently used water lubrication materials and successfully used in mechanical parts such as bearings or mechanical seals since Tomizawa and Fischer [1] reported that the friction coefficient of the against Si_3N_4 kits was less than 0.002 in water, and elucidated the water lubrication mechanism of the dynamic fluid pressure in 1987. Ceramic materials' excellent hardness and wear resistance, on the other hand, raise the processing complexity and expense. In contrast, composite materials of glass-ceramics not only integrate the advantages of ceramics and glass, such as suitable mechanical property, heat resistance and chemical resistance, but also possess high machinability in virtue of relatively softer glass compared with ceramics. Therefore, an increasing number of academics are paying particular attention to glass-ceramics. The anisotropy and thermal conductivity [2], thermal expansion coefficient and thermal shock resistance [3,4], vibration mode [5], afterglow effect [6] of glass-ceramics have all been researched, but the water lubrication performance has never been involved. Furthermore, Sasaki [7], Wong et al. [8] and Chen et al. [9], as well as other academics [10–16], focused on the water lubrication processes of composite ceramics, including SiC, Si_3N_4, Al_2O_3 and ZrO_2, but never reported on those of glass-ceramics.

As early as 1984, Sugita et al. [17] discovered that the amorphous hydrate $SiO_2{\cdot}H_2O$ was produced at the friction interface of two Si_3N_4 wafers in water, eventually, the wafer surfaces became smooth.

* Corresponding author. National Key Laboratory of Science and Technology on Helicopter Transmission, Nanjing University of Aeronautics and Astronautics, Nanjing, 210016, PR China.
** Corresponding author. National Key Laboratory of Science and Technology on Helicopter Transmission, Nanjing University of Aeronautics and Astronautics, Nanjing, 210016, PR China.
E-mail addresses: 18738593090@163.com (Z. Wang), 15937311032@163.com (J. Chen).

https://doi.org/10.1016/j.wear.2022.204440
Received 28 April 2022; Received in revised form 21 June 2022; Accepted 3 July 2022
Available online 13 July 2022

Tomizawa and Fischer [1] who first found the water lubrication characteristics of Si_3N_4 materials, also demonstrated that the $SiO_2{\cdot}H_2O$ was beneficial in lowering the friction coefficient between the Si_3N_4 surfaces. Saito et al. [13,14,18] investigated the chemical/mechanical wear ratios of Si_3N_4 by determining the quantity of ammonia tribochemically produced in water. A large constant for the regression curve of the chemical wear ratio showed a large chemical contribution to the wear of the material. Tribological analysis on the sliding surfaces of Si_3N_4 revealed that the observed low friction coefficient is attributable to the hydrate, and the hydrodynamic effect was due to water entrapped by hydroxide and hydrate and a model of the sliding surface is proposed. Chen et al. [19] explored the friction and wear of self-mated SiC and Si_3N_4 with different initial roughness sliding in water with a pin-on-disk. It was found that the wear mechanism for surface smoothening to obtain low friction was tribochemical wear. Xu and Kato [20] studied the formation of a tribochemical layer on silicon nitride sliding in water. The wear mode changes from mechanically dominated wear to tribochemically dominated wear as the sliding distance increases. The silica tribochemical layer is formed on the friction surface and reduces the friction. These studies further verified that the hydrodynamic lubrication processes of ceramics were realized by a hydrodynamic film generated by the tribochemical reaction between ceramics and water. Moreover, the surface-bound hydration layer consists of ceramic molecules and water molecules and the electrical double layer on the hydrodynamic film could be regarded as other hypotheses for the water lubrication mechanisms of ceramics. In 2002, Raviv and Klein [21] observed that the surface-bound hydration layer might form and maintain under high-speed fluid shear conditions *via* the rapid exchange of molecules [22]. By examining the link between the friction coefficient of the Si_3N_4-glass interface and the pH value in a phosphate solution, Li et al. [23] revealed that the hydrogen adsorbed on the Si_3N_4 surface could enhance the creation of the electrical double layer on the hydrodynamic film. In a nutshell, the ceramic water lubrication mechanisms may be explained in four ways as follows. 1) Hydrodynamic lubrication, which involves a water film flowing between two relatively slipping ceramic friction surfaces, entirely separating the ceramic friction pairs, and the contact load being balanced by dynamic fluid pressure [1,24,25]. 2) Boundary lubrication, based on the effects of the tribochemical reaction layer and the dynamic fluid pressure, that is, the colloidal silica film $SiO_2{\cdot}H_2O$ lubrication gradually takes the place of fluid dynamic pressure lubrication [8,9,18,20,26–29]. 3) Electrical double layer lubrication, the ceramic surface adsorbs a significant number of charged particles to form an electrical double layer due to the static electricity and van der Waals, and the layer plays a role in supporting the ceramic friction pair [12,20,22,30,31]. 4) Surface-bound hydration layer lubrication, hydrogen ions in the electrolyte solution can be absorbed on the ceramic surface with negative electricity through the protonation reaction, the surfaces of two ceramic friction pairs with the same electric charge repel each other to balance the contact load [21,22,30,32,33].

In fact, the hardness values of the glass-ceramics and the composite ceramics are larger than HRA80, and their anti-friction performance is outstanding. However, the melting points of the composite ceramics exceed 1400 °C which is almost twice as much as those of the glass-ceramics. The glass-ceramics have more advantages over the composite ceramics under the low speed and light load scenes. On the other hand, current water lubrication theories are primarily applied to ceramic materials such as SiC, Si_3N_4, Al_2O_3 and ZrO_2. The water lubrication mechanisms of glass-ceramics are not involved, in particular, the specific low friction process of glass-ceramics in the water environment is still unclear. Therefore, our custom-made γ-$LiAlSi_2O_6$ glass-ceramics were prepared for a ball and a wafer, and friction and wear tests were carried out. The water lubrication mechanisms of glass-ceramics in three different friction stages were clarified by contrasting dry and wet friction coefficients, abrasion losses and surface roughnesses of glass-ceramics, particle size distribution and zeta potential of wear debris along with time, which provided theoretical support for the application of γ-$LiAlSi_2O_6$ glass-ceramics in the water environment.

2. Materials and methods

2.1. Glass-ceramics

Our custom-made γ-$LiAlSi_2O_6$ glass-ceramic powders were pressed at 180 MPa for 5 min and made into a Φ 8 mm ball and a Φ 30mm × 1.4 mm wafer, respectively. The ball and the wafer were crystallized in a 700 °C thermostatic furnace (SJF1600, Boyuntong, China) for 2 h, and then cooled with the furnace after sintering.

The glass-ceramic samples were phase-wise investigated by an X-ray diffractor (D8 Advance A25, Bruker, USA), as shown in Fig. 1. The results indicate that the glass-ceramic samples were mainly made up of lithium aluminum silicate. According to the lattice map provided by Hongwei Shou and Yonghua Duan [2], the samples were γ-$LiAlSi_2O_6$ with a hexagonal crystal structure, as shown in Fig. 2.

2.2. Friction and wear tests

Before friction and wear tests, the glass-ceramic balls and wafers were lapped. The final surface roughness *Sa* values (i.e., the arithmetical average height of area) were the mean of nine measurements uniformly distributed throughout the lapped glass-ceramic surfaces, and they were about 142 nm as measured by an upright metallurgical microscope (DM2500 M, Lecia, Germany) and a white light interferometer (Contour GT-K0, Bruker, USA), as shown in Fig. 3. The lapped glass-ceramic surface was still covered with micro pits, which is related to the formation of a large number of micropores in the sintering process.

As seen in Fig. 4, the glass-ceramic ball and wafer could be considered friction pairs. The ball was held in place by a copper fixture and moved in X and Z directions through slide rails. The ball and the wafer had a contact force of 2 N. A stepless speed motor controlled the rotation rate of the wafer which was fixed at the bottom of a cylindrical container revolving with a disc. The average relative linear speed in the contact zone between the ball and the wafer was about 0.168 m/s. A torque sensor was also attached to the fixture to capture signals in real-time, and **Eq. (1)** was used to calculate the friction coefficient between the ball and the wafer.

$$\mu = \frac{f}{F_n} = \frac{T}{F_n L} \tag{1}$$

where μ and f are the friction coefficient and friction force (N) between

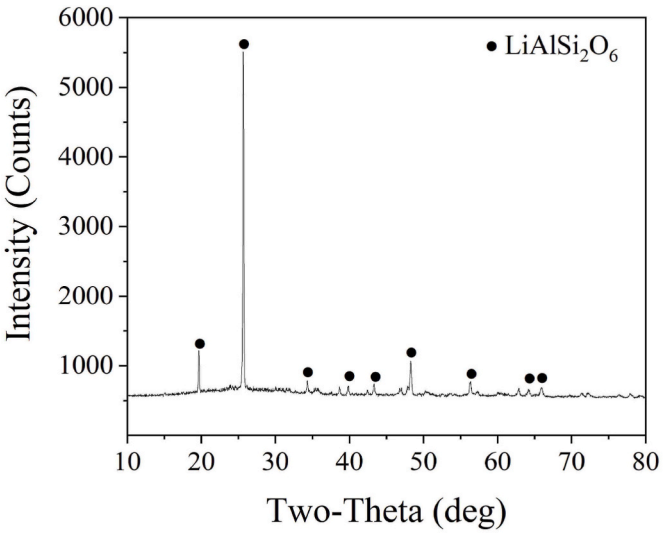

Fig. 1. XRD spectrum of γ-$LiAlSi_2O_6$.

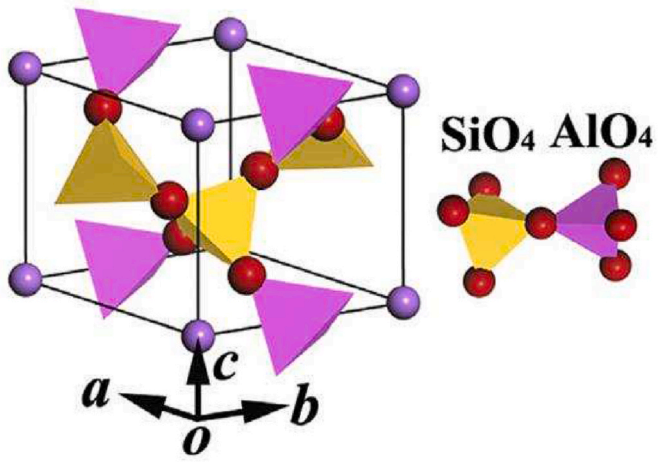

Fig. 2. Crystal structure of γ- $LiAlSi_2O_6$ and structure of SiO_4 tetrahedron and AlO_4 tetrahedron with a sharing O atom. The red and purple balls are oxygen and lithium atoms, respectively [2]. (For interpretation of the references to colour in this figure legend, the reader is referred to the Web version of this article.)

the ball and the wafer, respectively. F_n (N) and T (N•m) are the applied load and the torque on the ball, respectively. L (mm) is the distance from the center of the ball to the axis line of the wafer.

The dry and the wet friction and wear tests were separated into three stages, the first and second stages lasted 10 min, and the last stage lasted 40 min. To imitate a wet environment, 20 ml of deionized water (DIW) was decanted into the aluminum alloy container at the start of each wet friction test. To guarantee that the clamping locations were not changing, the ball and the wafer were immediately measured together with the fixture. The diameter of the wear area of glass-ceramic balls under different conditions was measured using a white light interferometer. To simplify the calculation, it is assumed that the wear areas are flattened. Therefore, the wear volume of the glass-ceramic spheres V is calculated as the sphere calculation Eq. (2) [34,35]:

$$V = \frac{\pi d^4}{64R} \tag{2}$$

where R is the radius of the ball and d is the diameter of the wear plane.

The area percentage of the pits on the wafer surface was obtained by calculating pixel values [36–38]. Wear debris was characterized by a Transmission Electron Microscope (TEM) equipped with an energy dispersive spectrometer (EDS) (HT7700, Hitachi, Japan). Wear debris size distribution trend was measured by a Zetasizer (Lab, Malvern, UK). The pH values in the water-based solution were monitored by a tester (PHS–3C, Leica, China) during wet friction processes.

3. Results and discussion

3.1. Variation of glass-ceramic friction coefficients in dry and wet conditions

In general, the whole friction and wear process is divided into three stages: running-in, stable and severe wear stage [39]. The dry and wet friction wear tests were conducted in three different groups, respectively. As demonstrated in Fig. 5, the fluctuation in the friction coefficient of glass-ceramics over time might represent the contact conditions of the friction pairs under various situations.

In the dry friction process, the friction coefficient was always more than 0.6, and its variation was violent. The dry running-in stage lasted 10 min, during which the asperities on the glass-ceramic surfaces slipped against each other and the total contact area was limited, resulting in high contact stress and shear force on the glass-ceramic asperities, and the friction coefficient fluctuated noticeably and rose straightly.

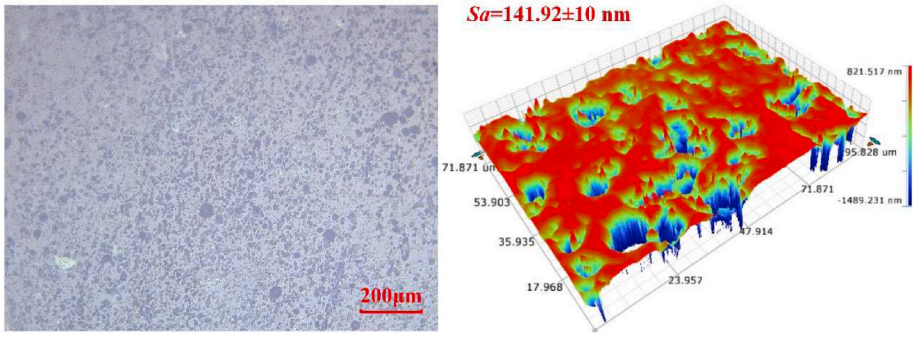

Fig. 3. Surface topography of the lapped γ-$LiAlSi_2O_6$ glass-ceramics.

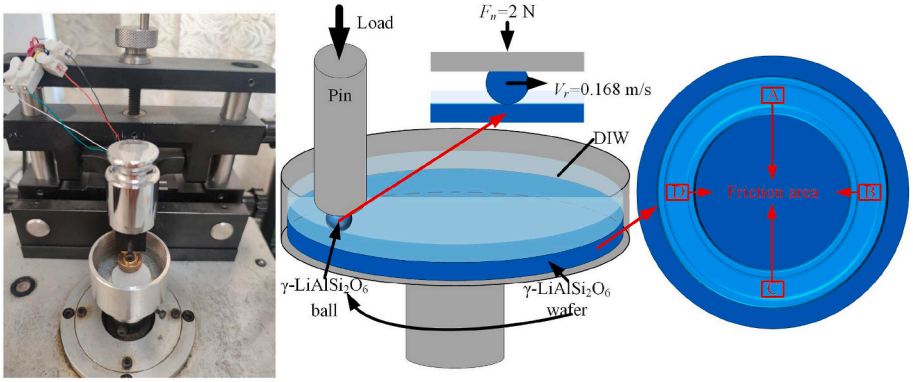

Fig. 4. Friction and wear setup and parameters.

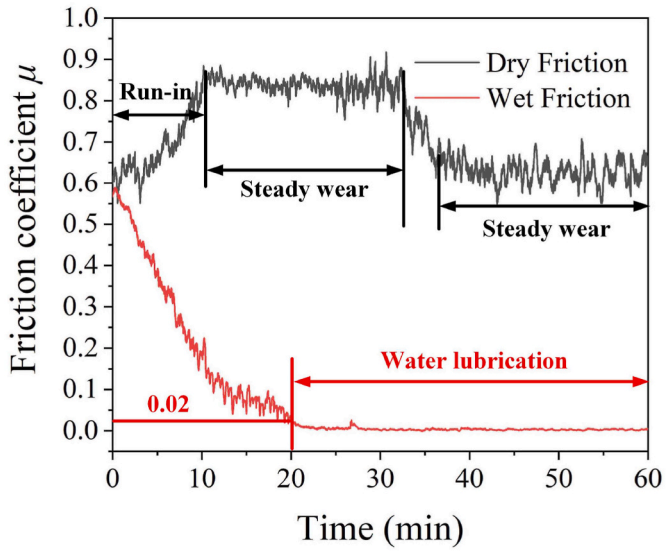

Fig. 5. Friction coefficient variation over time.

Afterward, the slipping glass-ceramic asperities were rapidly worn-flat in a short micro-cutting process, and the stable wear stage with a constant friction coefficient of 0.85 began at about 22 min and ended at 32 min. After a prolonged friction and wear process, the glass phase in glass-ceramics was softened due to friction heat, the softened glass phase formed a film layer on the friction pair surfaces (similar as Fig. 6 [40]) and played an anti-attrition role, therefore, the friction coefficient decreased and s eventually steadied at 0.6 which was similar as the initial point. By contrast, the wet friction coefficient dropped straightly down to 0.02 at 20 min, and subsequently stabilized until the end, indicating the water lubrication characteristic of glass-ceramics.

3.2. Variation in the topography of worn glass-ceramics

The low friction characteristics of glass-ceramics in the water environment were discovered by tracking the friction coefficient over time through dry and wet friction operations. The worn surface topography of glass-ceramic pairs was examined and compared in dry and wet friction processes to further investigate the reasons for water lubrication. The worn ball was exhibited in Fig. 7 along with the zone C on the wafer surface (Fig. 4), the wear volume of the ball and the area ratio of the pits on the wafer surface were determined and shown in Fig. 8. From Fig. 7,

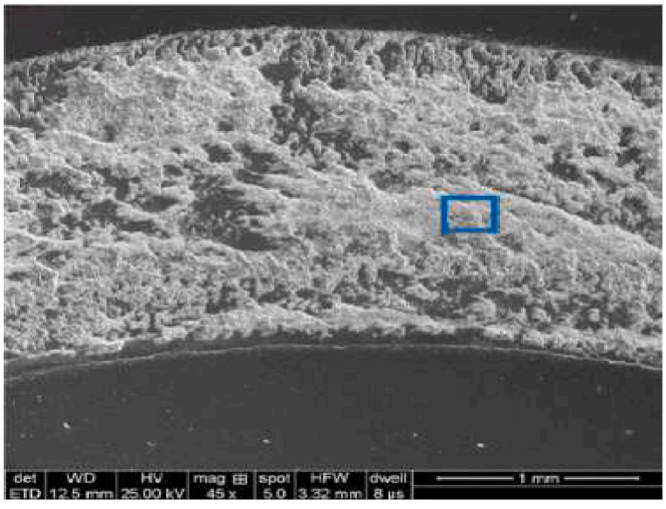

Fig. 6. SEM image of the sliding track on glass-ceramic [40].

the surface roughness values of the worn ball and the wafer first decrease and then increase along with the dry friction process, while the surface roughness on the slipping zones between the ball and the wafer dropped obviously.

The surface roughness of the glass-ceramic ball and the wafer spread out in the opposite directions in the dry or wet conditions, and the surface roughness decreased in the early stage of the dry friction process, but eventually increased significantly, as evidenced by the pits on the glass-ceramic wafer surface (Fig. 8 (b)). On contrary, over the whole friction and wear test, the wet surface roughness decreased dramatically, and the surface defects gradually reduced. Moreover, the initial wear rates of the two balls were nearly identical, however, the total wear volume of the dry glass-ceramic ball was almost twice that of the dry one. The wear volume of the dry ball rose significantly from 10 to 20 min, and then fell to a low value similar to that of the wet ball (Fig. 8 (a)). In the 10 min friction and wear tests, the contact number and area of the asperities on the rough glass-ceramic surfaces are restricted, resulting in a significant load on the contact area. According to Archard's law [41], the abrasion loss is proportional to the product of contact pressure and sliding velocity, so the wear rate is high. Typically, the asperities on the friction pair surfaces gradually wear and vanish throughout the continuous running-in stage. The surfaces smooth out and the total real contact area grows, which leads to a decrease in the wear rate of friction pairs. Obviously, the wet friction process is in line with the preceding law. However, the dry friction and wear process produces a lot of heat and that could cause severe contact point adhesion. Therefore, the friction coefficient, the wear rate, the surface defects and the surface roughness all go up. Shortly afterward, the glass phase is glazed in frictional heating, and the vitrification layer on the glass-ceramic surface acts as a lubricant, so the friction coefficient and the surface roughness are dropping (Fig. 7). By contrast, the friction heat is taken away by the water flow in the wet environment, and the water film is also a lubricant, which causes a decrease in the surface roughness, wear rate and friction coefficient.

3.3. Wear debris variation in friction and wear tests

The surface topography and the defect area ratio of the glass-ceramic wafer during the dry and wet friction and wear tests were compared in Section 3.2, the findings were opposite. The particular note is that the rough surface of the glass-ceramic wafer was initially covered with micro pits, however, the rough surface was smoothed down and the micro pits seemed to be filled in. Therefore, it is required to determine to classify and categorize wear debris which can fill the micro pits more effectively. Fig. 9 and Fig. 10 presented the morphology and EDS of wear debris created during the dry and wet friction and wear tests, respectively.

The bar and globular-like particles were produced during dry and wet friction processes, respectively, and dry wear debris is larger than wet ones. In addition, as demonstrated in Figs. 9 and 10 (a) (b), the weak Li element energy spectrum could not be shown, the percent of Al and Si atomics on the bar and globular-like particle surfaces were Al: Si ~ 1: 2, indicating that the particles were γ-$LiAlSi_2O_6$. The pull-out bar and globular-like particles are generated by the attrition and micro-fracture of the glass-ceramic ball and wafer, as evidenced by the surface topography of the scratch zone in Fig. 7. It is worth noting that the detected Al element energy spectrum of the nanoscale globular-like particles shown in Fig. 10 (c) is inconspicuous, and the silicon and oxygen atomic percentage is Si: O ~ 1: 2, therefore, the particles are most likely SiO_2.

Nano silica particles are more straightforward to fill micro holes or pores on the surface of the glass-ceramic wafer than bar and microscale globular-like particles, allowing for the formation of a smooth surface and a low friction coefficient. Therefore, the size and number of wear debris generated during dry and wet friction processes are necessary to measure and present in Fig. 11, respectively.

Throughout the test, the size distribution curves of the dry wear

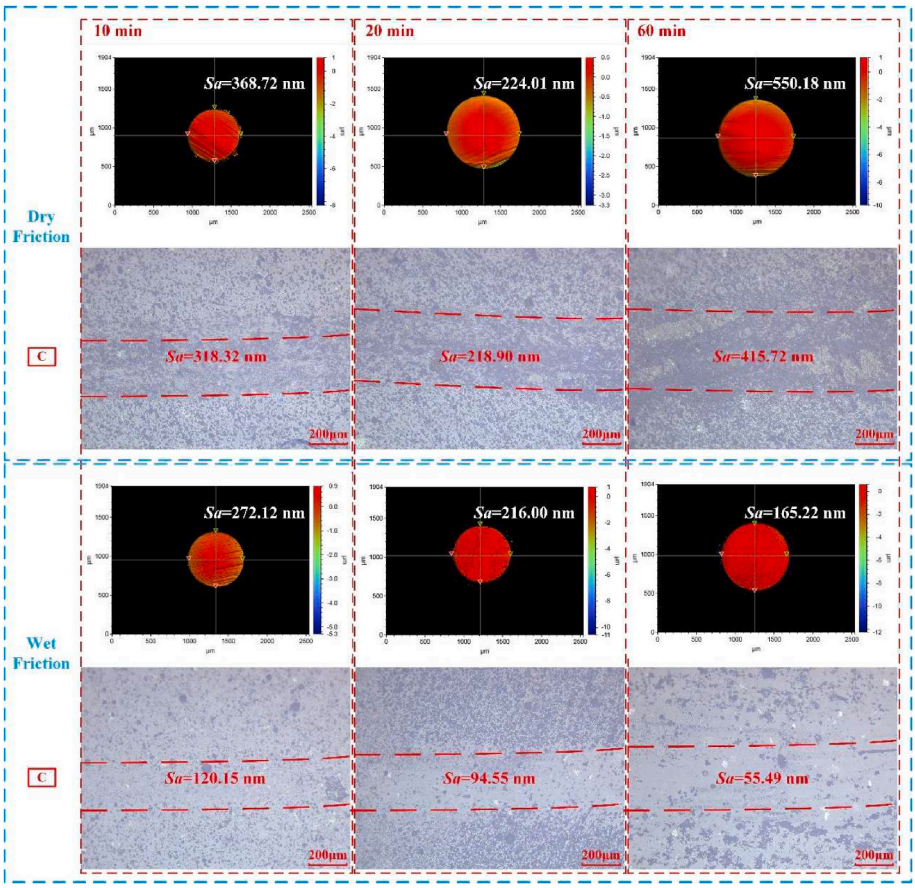

Fig. 7. Surface topography and roughness of γ- $LiAlSi_2O_6$ glass-ceramic ball and wafer at different dry or wet friction time points.

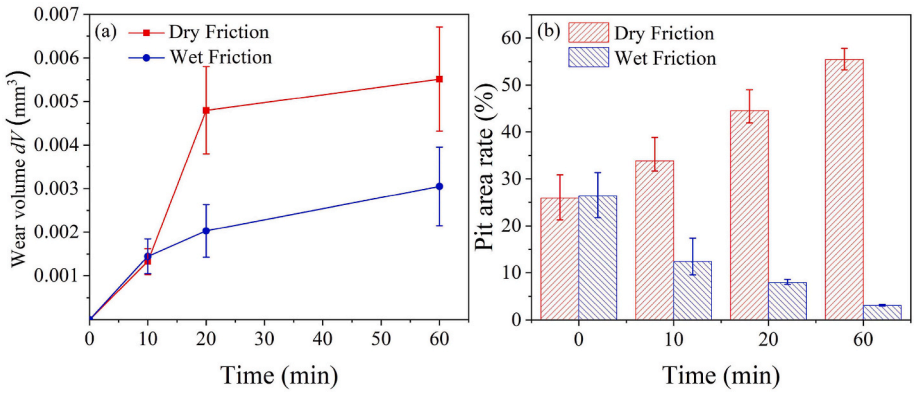

Fig. 8. (a) Wear volume of γ- $LiAlSi_2O_6$ glass-ceramic ball and (b) pit area radio of wafer at different dry or wet friction time points.

debris presented two pronounced peaks. The prominent peak shrank and the other peak broadened with the passage of time. In the initial stage of the dry friction process, the small real contact area between the ball and the wafer carried the high stress, therefore, the friction pairs were severely worn and even occurred micro-fracture. Moreover, the glass-ceramic surfaces were worn and torn by the large pull-out particles *via* three-body wear, resulting in additional micron and nano scale debris. As the ball surface was flattened (Fig. 7), the contact area increased and the contact stress decreased, the wear rate fell. The secondary debris breaking owing to the extrusion and shear, as well as the large pull-out particles rolling between the friction pairs, are prone to widening the particle size distribution range (Fig. 11 (a)). In the running-in stage of the wet friction, the wear debris in size of more than 200 nm only presented a single peak. Based on the above result and the analysis in Fig. 10 (a) (b), it can be judged that the wear debris is glass-ceramic particles. The single peak of wear debris turned into the double peaks during the stable wear stage, a large number of 100–200 nm debris could be judged to be silica particles based on discussing Fig. 10 (c), and the number continued to increase (Fig. 11 (b)). Moreover, the nano silica particles could effectively fill the micro pits and pores on the surface of the glass-ceramic wafer, which effectively reduced the wafer surface roughness (Fig. 7).

3.4. Water lubrication mechanism of glass-ceramics

The first stage of the water lubrication.

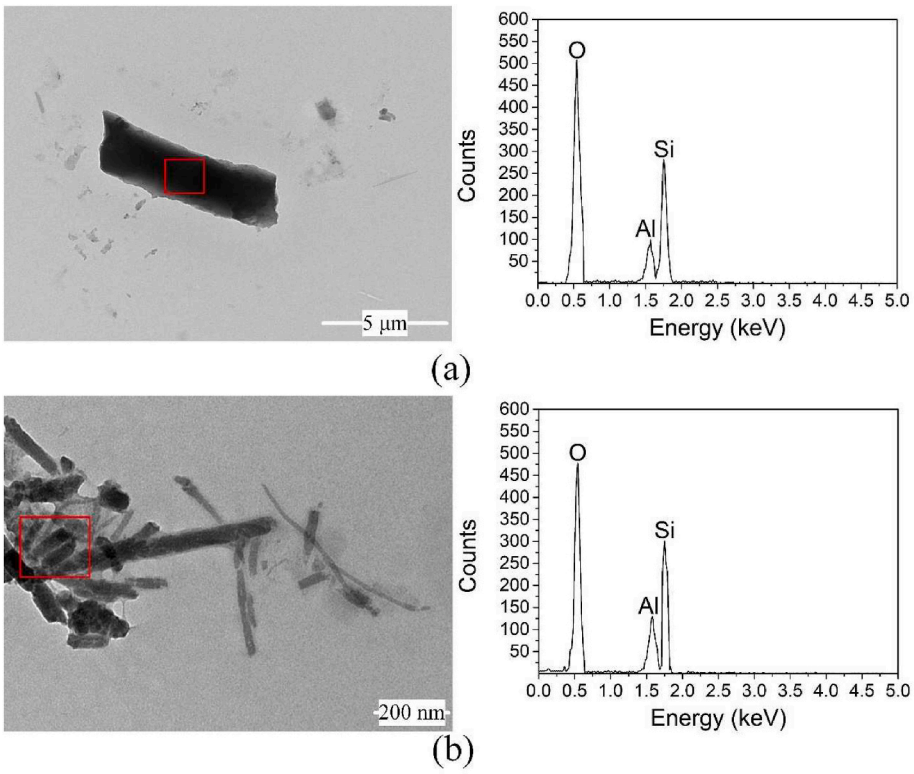

Fig. 9. TEM and EDS images of (a) microscale and (b) nanoscale bar wear debris during the dry friction process.

The friction and wear process between the glass-ceramic ball and wafer can be regarded as the ball cutting the wafer. In general, based on the rigid-plastic contact model, the cutting force F_p is defined as a total force on the rake face of the ball in the sliding direction. Fig. 12 shows how the force on the rake face is split.

On the surface of the wafer, the force F_p may be divided into the tangential force $F_{p,t}$ and the normal force $F_{p,n}$ as written as:

$$F_{p,t} = F_p|\cos\gamma| \tag{3}$$

$$F_{p,n} = F_p|\sin\gamma| \tag{4}$$

where γ is the negative rake angle of the ball.

The resultant friction force f_p along the ball rake face is calculated as follows:

$$f_p = \mu F_p \tag{5}$$

where μ is the friction coefficient between the ball and the wafer.

On the surface of the wafer, the friction force may be separated into the tangential force $f_{p,t}$ and the normal force $f_{p,n}$, as expressed as:

$$f_{p,t} = f_p|\sin\gamma| \tag{6}$$

$$f_{p,n} = f_p|\cos\gamma| \tag{7}$$

The total tangential force F_{pt} and the total normal force F_{pn} on the surface of the wafer are computed as:

$$F_{pt} = F_{p,t} + f_{p,t} = (|\cos\gamma| + \mu|\sin\gamma|)F_p \tag{8}$$

$$F_{pn} = F_{p,n} - f_{p,n} = (|\sin\gamma| - \mu|\cos\gamma|)F_p \tag{9}$$

Therefore, the cutting force ratio ε defined as the total normal force to the total tangential force can be calculated as:

$$\varepsilon = F_{pn} / F_{pt} = \frac{|\sin\gamma| - \mu|\cos\gamma|}{|\cos\gamma| + \mu|\sin\gamma|} = \frac{|\tan\gamma| - \mu}{1 + \mu|\tan\gamma|} = \frac{1}{\mu} - \frac{\mu^2 + 1}{\mu(1 + \mu|\tan\gamma|)} \tag{10}$$

Due to the wear of the glass-ceramic ball in the friction test, the negative rake angle of the ball constantly drops down to close to −90°, Eq. (10) can be simplified to $\varepsilon \approx 1/\mu$. Thus, the friction coefficient between the glass-ceramic ball and the wafer decreases as the cutting force ratio increases, which is also in accord with the works of literatures [42, 43]. Fig. 5 shows that the wet friction process conforms to the above law, while the friction coefficient increases in the early stage of the dry friction test. This is due to the micro-fracturing of the glass-ceramics in the friction and wear process, and the rake face of the ball is broken into several new rake faces (Fig. 12 (a)), causing the cutting force ratio to fluctuate or even decrease, while the friction coefficient reveals the opposite. In addition, the wafer can be efficiently cut by the ball with just a primary rake face and a large incident cutting angle or multi-cutting edges [44–46]. Therefore, the wear volume of the ball increases from 10 to 20 min during the dry friction process (Fig. 8 (a)), and the defects on the wafer surface (Fig. 8 (b)) and the surface roughness of glass-ceramics experience the parallel development (Fig. 7).

Although the cutting force ratio model explains the variation of the friction coefficient between the glass-ceramic ball and wafer in the dry friction process, the lubrication mechanism of the wet friction cannot be fully clarified. In fact, γ-$LiAlSi_2O_6$ glass ceramics can react with water and translate into colloidal silica in frictional heating, as shown in **Eq. (11)** [47].

$$3LiAlSi_2O_6 + 2H_2O + K^+ \rightarrow KAl_2(AlSi_3)O_{10}(OH)_2 + 3Li^+ + 3SiO_2 + 2OH^- \tag{11}$$

where K^+ is a kind of cation, the generation consisting of silica and OH^- is soluble silicic acid.

To be precise, the Li atom in a γ-$LiAlSi_2O_6$ cell (Fig. 2) can be regarded as an ion in the gap, while Al, Si, and O atoms form the skeleton of the cell. There is the polyhedron of {SiO4} units connected with co-vertexes such as Al atoms. The reaction shown in **Eq. (11)** belongs to a hydrolysis process, and the generation corresponding to the Si element is the ortho-silicic acid $Si(OH)_4$. Moreover, the $Si(OH)_4$ produced in the

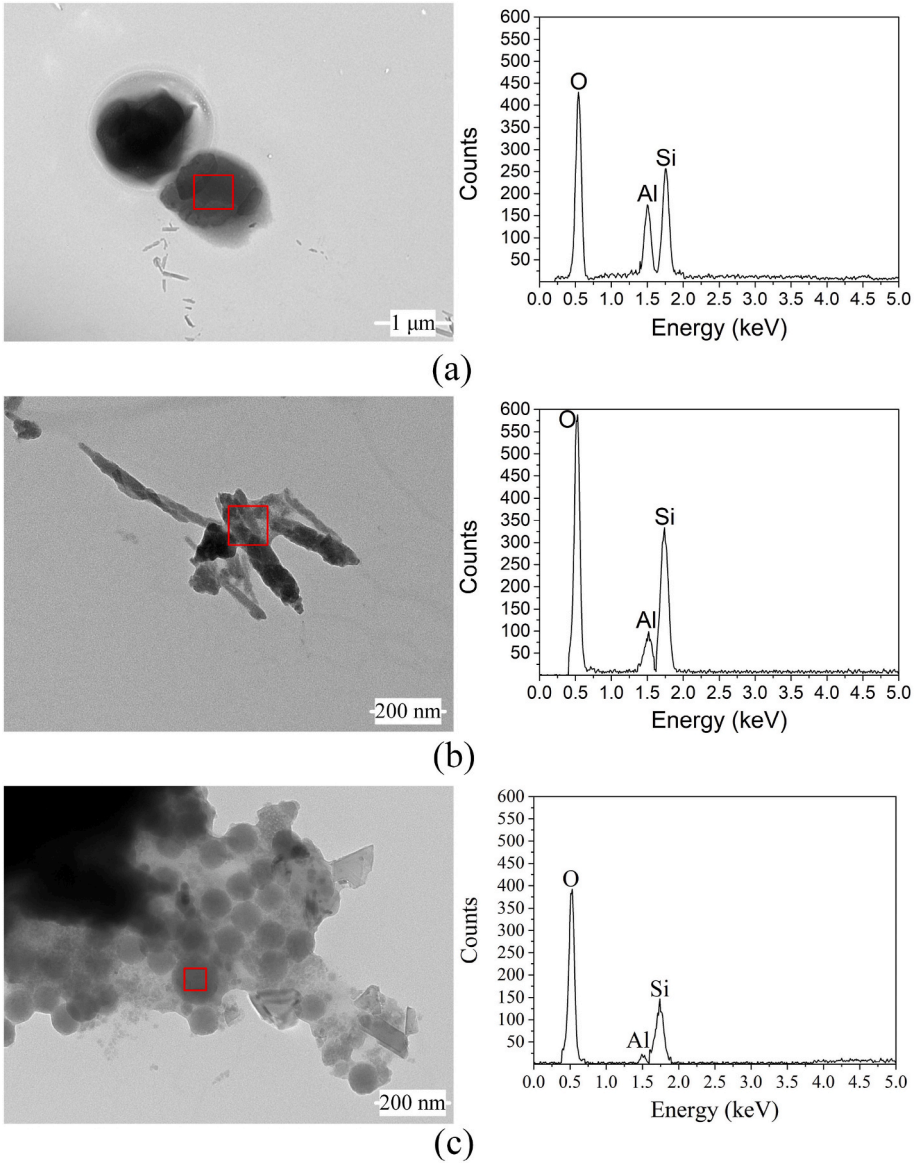

Fig. 10. TEM and EDS images (a) microscale nanoscale globular-like, (b) nanoscale bar wear debris and (c) nanoscale globular-like wear debris during the wet friction process.

wet friction process is heated by the electron ray, and decomposed to SiO_2 [48], which leads to the TEM and EDS images shown in Fig. 10 (c).

3.4.1. *The second stage of the water lubrication*

With the increase of the sliding distance in the running-in stage of the wet friction process, the contact area between the ball and the wafer becomes largens, the contact stress spreads, and the chemical wear is instead of mechanical wear gradually. This is mainly because the mechanical friction between the glass-ceramic ball and wafer is weakened when the contact pressure and friction surface roughness are lowered. The glass-ceramics are induced by extrusion and impact, pass through and break along their crystals, and then react with water in frictional heating, resulting in an agglomerated $Si(OH)_4$ film progressively growing and broadening on the glass-ceramic surfaces, which is an interactive process of micro-fracturing, oxidation and hydration of glass-ceramic materials [21]. The frictional chemical reaction occurs on the local interface between the glass-ceramic ball and wafer, and a colloidal silica layer is generated and expands to a hydration bond network to achieve the lubrication effect, as illustrated in Fig. 13.

3.4.2. *The final stage of the water lubrication*

Yamakirin et al. [49] investigated the effects of laser surface texturing on the friction behavior of silicon nitride under lubrication with water. They found that in a case of small dimple diameter textured surface, the dimples were buried with the wear debris as shown in Fig. 14.

Similarly, the glass-ceramic ball and wafer occur Hertz contact in the initial stage of the wet friction process, the contact area gradually increases along with time, meanwhile, a large number of nanoscale colloidal silica particles (Figs. 10 and 11 (b)) generated by the frictional chemical reaction fill the pits on the contact area. Therefore, the rough contact surface is flattened and smoothed (Fig. 7), and the applied load on the wafer is balanced by a hydrodynamic force brought from a flowing water film. Furthermore, the friction coefficient drops down to 0.02 when the minimum water film thickness is larger than the composite roughness of the two friction surfaces [20]. The above is the whole hydrodynamic lubrication process. Furthermore, Wang et al. [50, 51] studied the effect of laser texturing of Si_3N_4 surface on the critical load for the transition of water lubrication mode from hydrodynamic to mixed and optimized the surface texture for silicon carbide sliding in

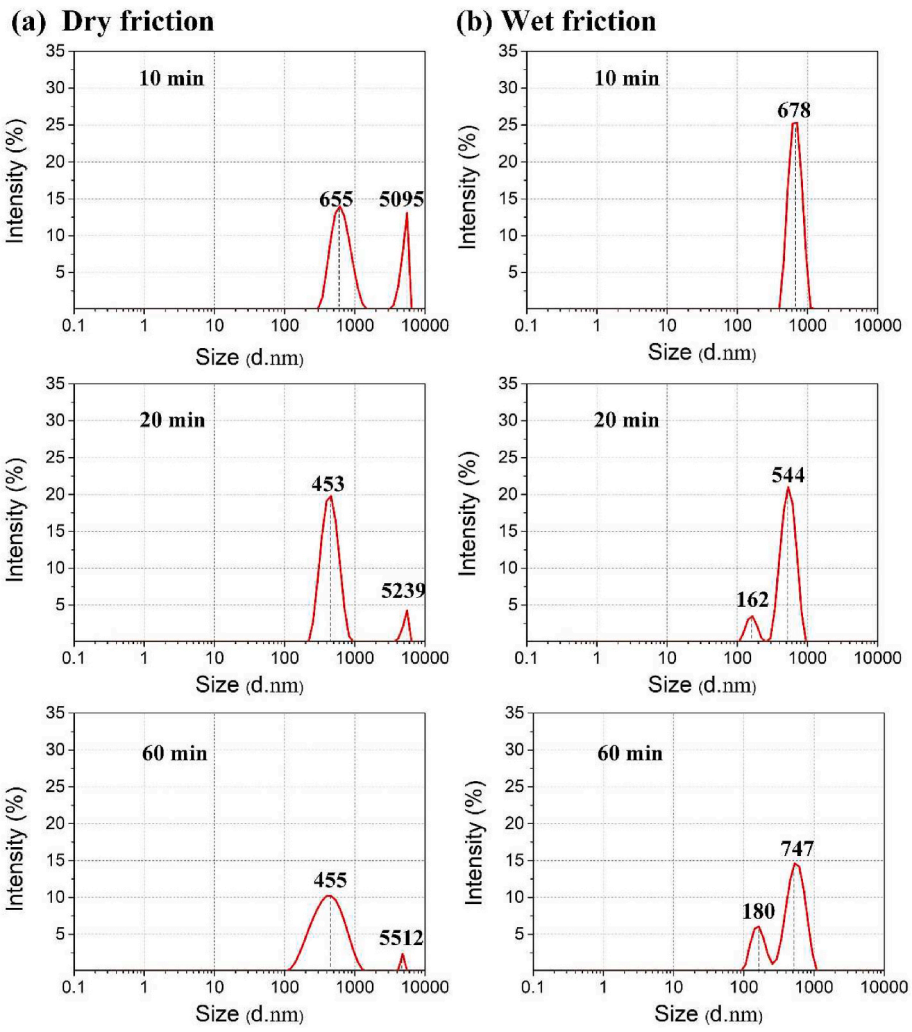

Fig. 11. Size distribution variation of wear debris during dry or wet friction process.

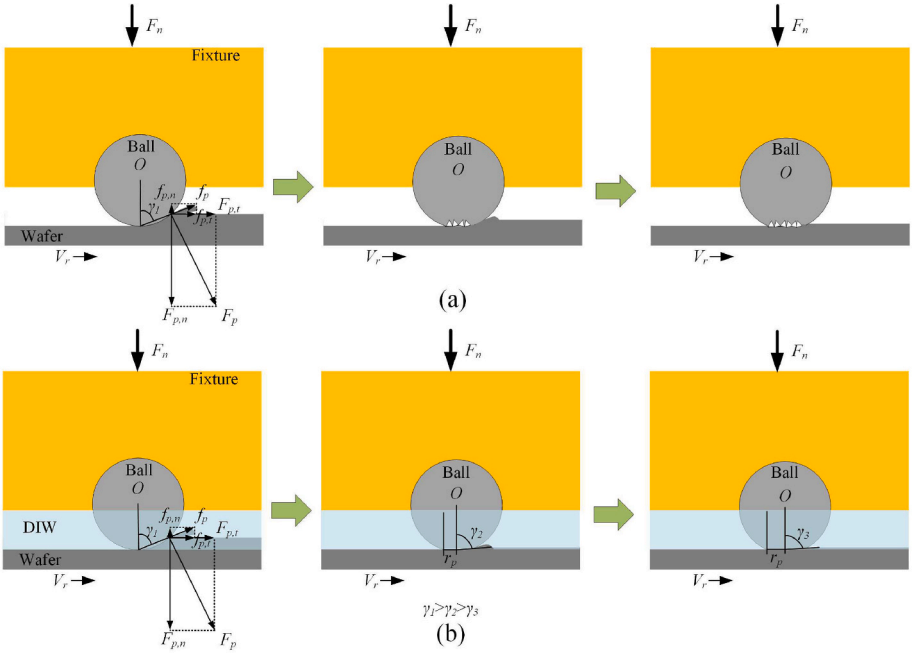

Fig. 12. Schematic diagrams of (a) dry or (b) wet friction in a γ- $LiAlSi_2O_6$ glass-ceramic ball sliding a wafer process.

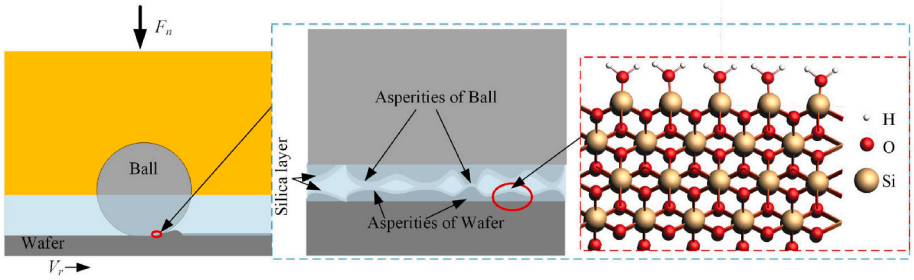

Fig. 13. Boundary lubrication of the colloidal silica layer in the wet friction process.

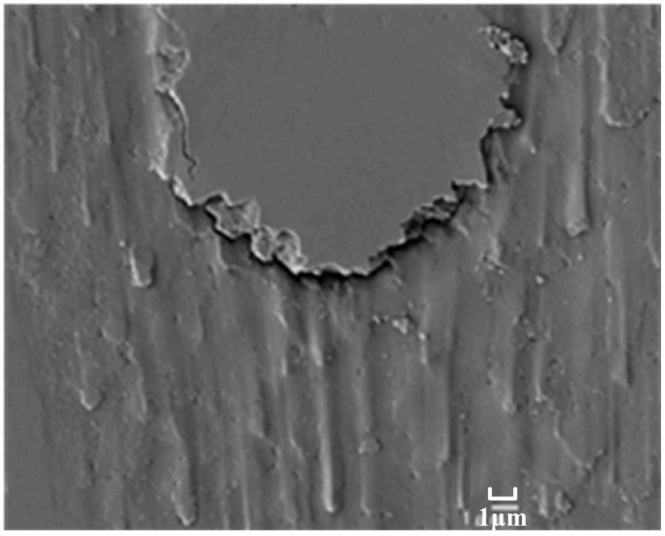

Fig. 14. SEM microphotographs of the textured surfaces after the sliding test [49].

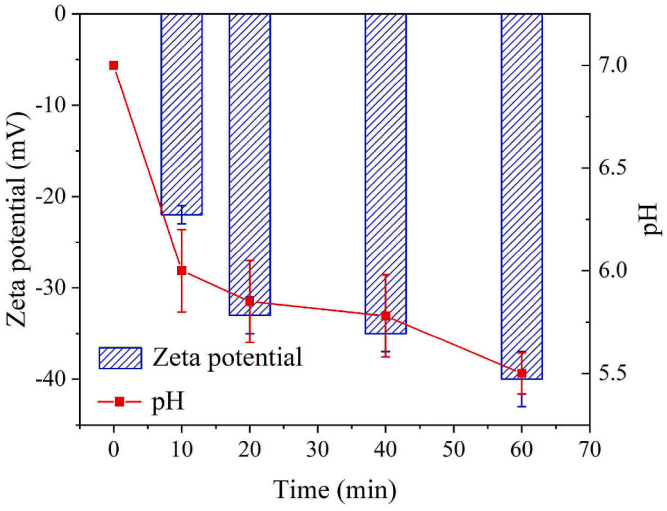

Fig. 15. Zeta potential of wet wear debris and pH values of water-based suspension over time.

water. These studies prove that surface texturing was an effective means to improve the tribological performances of sliding surfaces, enhanced hydrodynamic lubrication and collected debris.

In addition, the Zeta potential of the wet wear debris and the pH values of water-based suspension over time were measured and displayed in Fig. 15. The lubrication mechanism in the later stage of the wet friction process is clarified as shown in Fig. 16.

The Zeta potential and the pH values presented the opposite trend, which is justifiable on the weak ionization of $Si(OH)_4$. The zero charge point of SiO_2 exists at pH = 2.5, therefore, the Zeta potential of the silica particles is positive if the pH value of the water-based suspension is below 2.5, the opposite the colloidal silica is negatively charged [52]. The diffusion layer of the colloidal silica generated by the tribochemistry effect is positively charged, therefore, the colloidal silica film is adsorbed onto the glass-ceramic surface with negative electricity, and an electrical double layer is formed. The glass-ceramic ball and wafer surface are adsorbed with colloidal silica, which leads to the same-charge exclusion and hydration effects. The above is the electrical double lubrication process.

Eventually, no matter the hydrodynamic or electrical double lubrication on the friction interface can provide a rising force that counteracts the applied load, and the real contact area between the glass-ceramic ball and wafer declines, resulting in the decrease of the shear force perpendicular to the friction interface. According to **Eq. (10)**, it can be determined that the friction coefficient reduces first and then stabilize at about 20 min (Fig. 5). In the water, the formed water film can play the role of lubrication and isolation of friction pairs' direct contact. The ortho-silicic acid $Si(OH)_4$ generated in this process may improve the viscosity of water, further increase the carrying capacity of water film, and thus play a better lubrication effect than water film [53–55]. The interactive lubrication effects of the electrical double layer and the dynamic fluid pressure ensure that the wet friction coefficient of the glass-ceramics is constant below 0.02.

4. Conclusion

A custom-made γ-$LiAlSi_2O_6$ glass-ceramics are prepared for a ball and a wafer which were used to carry out friction and wear tests in this paper. The water lubrication mechanisms of glass-ceramics in three different friction stages are summarized as follows:

(1) In the initial stage of the wet friction process, the stress on the contact area between the glass-ceramic ball and wafer is concentrated, the rake face of the ball is rapidly worn, and the cutting force ratio increases, while the friction coefficient decreases. At the same time, the friction interface forms colloidal silica with a lubrication function.

(2) In the middle stage of the wet friction process, the friction area increases, the contact stress spreads, and mechanical wear on the friction interface translates to chemical wear. The worn glass-ceramic materials experience a synchronous process of microfracturing, oxidation and hydration, forming a colloidal silica film and a hydration bond network.

(3) In the later stage of the wet friction process, the nanoscale colloidal silica generated by the frictional chemical reaction can efficiently fill the pits on the glass-ceramic surface. The hydrodynamic film between the smooth surfaces of the ball and wafer plays a lubrication role. At the same time, the diffusion layers of the colloidal silica film adsorbed on the friction interface are

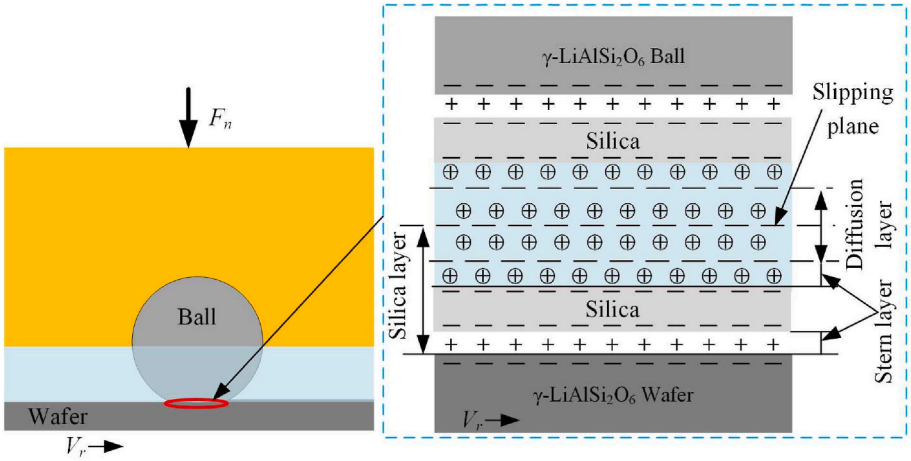

Fig. 16. Water lubrication mechanism of the stable low-friction process of γ- $LiAlSi_2O_6$ glass-ceramics.

positively charged, the ball and wafer repel each other, and the repulsive force can set off a part of the contact load.

Author statement

Yanan Peng: Conceptualization, Methodology, Software, Validation, Formal analysis, Investigation, Writing - Original Draft, Writing - Review & Editing, Visualization.

Zeyu Wang*: Conceptualization, Methodology, Writing - Review & Editing, Supervision.

Yuantao Fu: Software, Validation.

Xiaoqin Zhang: Writing - Review & Editing.

Jiapeng Chen*: Conceptualization, Methodology, Resources, Writing - Review & Editing, Supervision, Funding acquisition, Validation.

Declaration of competing interest

The authors declare that they have no known competing financial interests or personal relationships that could have appeared to influence the work reported in this paper.

Data availability

Data will be made available on request.

Acknowledgment

The paper is supported by National Natural Science Foundation of China (Grant No. U20A20293).

References

[1] H. Tomizawa, T.E. Fischer, Friction and wear of silicon nitride and silicon carbide in water: hydrodynamic lubrication at low sliding speed obtained by tribochemical wear, Taylor & Francis 30 (1) (1987) 41–46. https://doi:10.1080/0569819870898 1728.

[2] H. Shou, Y. Duan, Anisotropic elasticity and thermal conductivities of (α, β, γ)-$LiAlSi_2O_6$ from the first-principles calculation, J. Alloys Compd. 756 (2018) 40–49. https://doi:10.1016/j.jallcom.2018.05.040.

[3] E. Kleebusch, C. Patzig, T. Höche, C. Rüssel, Effect of the concentrations of nucleating agents ZrO2 and TiO_2 on the crystallization of Li_2O–Al_2O_3–SiO_2 glass: an X-ray diffraction and TEM investigation, J. Mater. Sci. 51 (22) (2016) 10127–10138. https://doi:10.1007/s10853-016-0241-9.

[4] E. Kleebusch, C. Patzig, T. Höche, C. Rüssel, Phase formation during crystallization of a Li_2O-Al_2O_3-SiO_2 glass with ZrO_2 as nucleating agent–An X-ray diffraction and (S)TEM-study, Ceram. Int. 43 (13) (2017) 9769–9777. https://doi:10.1016/j.ceramint.2017.04.153.

[5] A.A. Kaminskii, L. Bohatý, E. Libowitzky, H. Rhee, O. Lux, H.J. Eichler, R. Kleinschrodt, H. Yoneda, A. Shirakawa, P. Becker, Spodumene, α-$LiAlSi_2O_6$–A new natural SRS-active crystal with three $\chi^{(3)}$-promoting vibrational modes, Opt. Mater. 78 (2018) 235–246. https://doi: 10.1016/j.optmat.2018.02.022.

[6] M. Czaja, R. Lisiecki, M. Kądziołka-Gaweł, A. Winiarski, T. Krzykawski, The afterglow effect of Mn-bearing natural $LiAlSi_2O_6$ spodumene crystals, Opt. Mater. 96 (2019), 109321. https://doi: 10.1016/j.optmat.2019.109321.

[7] S. Sasaki, The effects of the surrounding atmosphere on the friction and wear of alumina, zirconia, silicon carbide and silicon nitride, Wear 134 (1) (1989) 185–200. https://doi:10.1016/0043-1648(89)90068-9.

[8] H.C. Wong, N. Umehara, K. Kato, Frictional characteristics of ceramics under water-lubricated conditions, Tribol. Lett. 5 (4) (1998) 303–308. https://doi:10.1023/A:1019174615499.

[9] M. Chen, K. Kato, K. Adachi, The difference in running-in period and friction coefficient between self-mated Si_3N_4 and SiC under water lubrication, Tribol. Lett. 11 (1) (2001) 23–28. https://doi: 10.1023/A:1016621929078.

[10] Y. Imada, K. Kamamura, F. Honda, K. Nakajima, The tribological reaction accompanying friction and wear of silicon nitride containing titanium nitride, J. Tribol. 114 (2) (1992) 230–235. https://doi: 10.1115/1.2920878.

[11] A. Lipp, K.A. Schwetz, K. Hunold, Hexagonal boron nitride: fabrication, properties and applications, J. Eur. Ceram. Soc. 5 (1) (1989) 3–9. https://www.sciencedirect.com/science/article/pii/0955221989900034.

[12] V. Ferreira, H.N. Yoshimura, A. Sinatora, Ultra-low friction coefficient in alumina–silicon nitride pair lubricated with water, Wear 296 (1–2) (2012) 656–659. https://doi:10.1016/j.wear.2012.07.030.

[13] T. Saito, Y. Imada, F. Honda, Chemical influence on wear of Si_3N_4 and hBN in water, Wear 236 (1–2) (1999) 153–158. https://doi:10.1016/S0043-1648(99)00270-7.

[14] T. Saito, T. Hosoe, F. Honda, Chemical wear of sintered Si_3N_4, hBN and Si_3N_4–hBN composites by water lubrication, Wear 247 (2) (2001) 223–230. https://doi:10.1016/S0043-1648(00)00539-1.

[15] R.P.D. Oliveira, E.D. Santos, T. Cousseau, A. Sinatora, Effect of pH on wear and friction of silicon nitride sliding against alumina in water, Tribol. Int. 90 (2015) 356–361. https://doi:10.1016/j.triboint.2015.04.003.

[16] Y. Hibi, Y. Enomoto, Lubrication of Si_3N_4 and $A1_2O_3$ in water with and without addition of silane coupling agents in the range of 0.05-0.10 mol/l, Tribol. Int. 28 (2) (1995) 97–105. https://doi:10.1016/0301-679X(95)92699-6.

[17] T. Sugita, K. Ueda, Y. Kanemura, Material removal mechanism of silicon nitride during rubbing in water, Wear 97 (1) (1984) 1–8. https://doi:10.1016/0043-1648(84)90076-0.

[18] T. Saito, Y. Imada, F. Honda, An analytical observation of the tribochemical reaction of silicon nitride sliding with low friction in aqueous solutions, Wear 205 (1) (1997) 153–159. https://doi:10.1016/S0043-1648(96)07287-0.

[19] M. Chen, K. Kato, K. Adachi, Friction and wear of self-mated SiC and Si_3N_4 sliding in water, Wear 250 (1) (2001) 246–255. https://doi:10.1016/S0043-1648(01)00648-2.

[20] J. Xu, K. Kato, Formation of tribochemical layer of ceramics sliding in water and its role for low friction, Wear 245 (1) (2000) 61–75. https://doi:10.1016/S0043-1648(00)00466-X.

[21] U. Raviv, Fluidity of bound hydration layers, Science 297 (5586) (2002) 1540–1543. https://doi:10.1126/science.1074481.

[22] J. Li, C. Zhang, J. Luo, Superlubricity behavior with phosphoric acid–water network induced by rubbing, Langmuir 27 (15) (2011) 9413–9417. https://doi:10.1021/la201535x.

[23] J. Li, C. Zhang, J. Luo, Effect of pH on the liquid superlubricity between Si_3N_4 and glass achieved with phosphoric acid, RSC Adv. 4 (86) (2014) 45735–45741. https://doi:10.1039/C4RA04970E.

[24] L. Jordi, C. Iliev, T.E. Fischer, Lubrication of silicon nitride and silicon carbide by water: running in, wear and operation of sliding bearings, Tribol. Lett. 17 (3) (2004) 367–376. https://doi:10.1023/B:TRIL.0000044485.77019.fb.

[25] S.R. Hah, C.B. Burk, T.E. Fischer, Surface quality of tribochemically polished silicon nitride, J. Electrochem. Soc. 146 (4) (1999) 1505–1509. https://doi:10.1149/1.1391795.
[26] X. Wang, K. Kato, K. Adachi, Running-in effect on the load-carrying capacity of a water-lubricated SiC thrust bearing, in: ARCHIVE Proceedings of the Institution of Mechanical Engineers Part J Journal of Engineering Tribology 1946-1996(vols 208-210), vol. 219, 2005, pp. 117–124, 2, https://doi:10.1243/135065005X9727.
[27] F. Zhou, X. Wang, K. Adachi, K. Kato, Influence of normal load and sliding speed on the tribological property of amorphous carbon nitride coatings sliding against Si_3N_4 balls in water, Surf. Coating. Technol. 202 (15) (2008) 3519–3528. https://doi:10.1016/j.surfcoat.2007.12.025.
[28] J. Xu, K. Kato, T. Hirayama, The transition of wear mode during the running-in process of silicon nitride sliding in water, Wear 205 (1) (1997) 55–63. https://doi:10.1016/S0043-1648(96)07283-3.
[29] X. Wang, K. Kato, K. Adachi, The critical condition for the transition from HL to ML in water-lubricated SiC, Tribol. Lett. 16 (4) (2004) 253–258. https://doi:10.1023/B:TRIL.0000015200.37141.f5.
[30] J. Li, C. Zhang, L. Sun, X. Lu, J. Luo, Tribochemistry and superlubricity induced by hydrogen ions, Langmuir 28 (45) (2012) 15816–15823. https://doi:10.1021/la303897x.
[31] L. Sun, C. Zhang, J. Li, Y. Liu, J. Luo, Superlubricity of Si_3N_4 sliding against SiO_2 under linear contact conditions in phosphoric acid solutions, Sci. China Technol. Sci. 56 (7) (2013) 1678–1684. https://doi:10.1007/s11431-013-5257-7.
[32] J. Li, L. Ma, S. Zhang, C. Zhang, Y. Liu, J. Luo, Investigations on the mechanism of superlubricity achieved with phosphoric acid solution by direct observation, J. Appl. Phys. 114 (11) (2013), 114901. https://doi:10.1063/1.4821063.
[33] J. Li, C. Zhang, L. Ma, Y. Liu, J. Luo, Superlubricity achieved with mixtures of acids and glycerol, Langmuir 29 (1) (2013) 271–275. https://doi:10.1021/la3046115.
[34] F. Zhou, K. Kato, K. Adachi, Friction and wear properties of CNx/SiC in water lubrication, Tribol. Lett. 18 (2) (2005) 153–163. https://doi:10.1007/s11249-004-1771-x.
[35] R. Wsche, D. Klaffke, Ceramic particulate composites in the system SiC-TiC-TiB_2 sliding against SiC and Al_2O_3 under water, Tribol. Int. 32 (4) (1999) 197–206. https://doi:10.1016/S0301-679X(99)00033-X.
[36] Z. Qiu, H. Fang, Y. Zhang, Y. He, Measurement of plant leaf area using image processing techniques, Proc. SPIE-Int. Soc. Opt. Eng. 6027 (2006) 885–891. https://doi:10.1117/12.668331.
[37] Q. Hu, H. Yin, M.A. Friedl, L. You, Z. Li, H.W. Tang, Integrating coarse-resolution images and agricultural statistics to generate sub-pixel crop type maps and reconciled area estimates, Remote Sens. Environ. 258 (2021), 112365. https://doi:10.1016/j.rse.2021.112365.
[38] J. Han, Z. Zhang, J. Cao, Y. Luo, Mapping Rapeseed Planting Areas Using an Automatic Phenology- and Pixel-Based Algorithm (APPA) in Google Earth Engine, The Crop Journal, 2022, https://doi.org/10.1016/j.cj.2022.04.013.
[39] S. Jahanmir, T.E. Fischer, Friction and wear of silicon nitride lubricated by humid air, water, hexadecane and hexadecane + 0.5 percent stearic acid, Tribol. Trans. 31 (1) (1988) 32–43. https://doi:10.1080/10402008808981795.
[40] J. Zhou, H. Xu, C. Zhu, W. Ai, X. Liu, K. Liu, High-temperature friction characteristics of N-BK7 glass and their correlation with viscoelastic loss modulus, Ceram. Int. 47 (15) (2021) 21414–21424. https://doi:10.1016/j.ceramint.2021.04.151.
[41] J.F. Archard, Contact and rubbing of flat surfaces, J. Appl. Phys. 24 (8) (1953) 981–988. https://doi:10.1063/1.1721448.
[42] J. Chen, N. Zhu, F. Niu, Y. Peng, J. Su, Y. Zhu, Influence of agglomerated diamond abrasive wear on sapphire material removal behavior, Diam. Relat. Mater. 108 (2020), 107965. https://doi:10.1016/j.diamond.2020.107965.
[43] C. Dai, W. Ding, J. Xu, Y. Fu, T. Yu, Influence of grain wear on material removal behavior during grinding nickel-based superalloy with a single diamond grain, Int. J. Mach. Tool Manufact. 113 (2017) 49–58. https://doi:10.1016/j.ijmachtools.2016.12.001.
[44] J. Chen, Y. Zhu, J. Wang, Y. Peng, J. Yao, S. Ming, Relationship between mechanical properties and processing performance of agglomerated diamond abrasive compared with single diamond abrasive, Diam. Relat. Mater. 100 (2019), 107595. https://doi:10.1016/j.diamond.2019.107595.
[45] N. Rüttimann, M. Roethlin, S. Buhl, K. Wegener, Simulation of hexa-octahedral diamond grain cutting tests using the SPH method, Procedia CIRP 8 (2013) 322–327, in: https://doi:10.1016/j.procir.2013.06.110.
[46] J. Chen, Y. Peng, Z. Wang, T. Sun, J. Su, D. Zuo, Y. Zhu, Tribological effects of loose alumina abrasive assisted sapphire lapping by a fixed agglomerated diamond abrasive pad (FADAP), Mater. Sci. Semicond. Process. 143 (2022), 106556. https://doi:10.1016/j.mssp.2022.106556.
[47] J. Graham, Some notes on α-spodumene, $LiAlSi_2O_6$, Am. Mineral. 60 (9–10) (1975) 919–923.
[48] E. Kleebusch, C. Patzig, T. Höche, C. Rüssel, The evidence of phase separation droplets in the crystallization process of a Li_2O-Al_2O_3-SiO_2 glass with TiO_2 as nucleating agent–An X-ray diffraction and (S)TEM-study supported by EDX-analysis, Ceram. Int. 44 (3) (2018) 2919–2926. https://doi:10.1016/j.ceramint.2017.11.040.
[49] H. Yamakiri, S. Sasaki, T. Kurita, N. Kasashima, Effects of laser surface texturing on friction behavior of silicon nitride under lubrication with water, Tribol. Int. 44 (5) (2011) 579–584. https://doi:10.1016/j.triboint.2010.11.002.
[50] X. Wang, K. Kato, K. Adachi, K. Aizawa, The effect of laser texturing of SiC surface on the critical load for the transition of water lubrication mode from hydrodynamic to mixed, Tribol. Int. 34 (10) (2001) 703–711. https://doi:10.1016/S0301-679X(01)00063-9.
[51] X. Wang, K. Adachi, K. Otsuka, K. Kato, Optimization of the surface texture for silicon carbide sliding in water, Appl. Surf. Sci. 253 (4) (2006) 1282–1286. https://doi:10.1016/j.apsusc.2006.01.076.
[52] G.A. Parks, P.L. Bruyn, The zero point of charge of oxides, J. Phys. Chem. 66 (6) (1962) 967–973. https://doi:10.1021/j100812a002.
[53] G.T.Y. Wan, P. Kenny, H.A. Spikes, Elastohydrodynamic properties of water-based fire-resistant hydraulic fluids, Tribol. Int. 17 (6) (1984) 309–315, https://doi.org/10.1016/0301-679X(84)90093-8.
[54] Y. Shi, I. Minami, M. Grahn, M. Björling, R. Larsson, Boundary and elastohydrodynamic lubrication studies of glycerol aqueous solutions as green lubricants, Tribol. Int. 69 (1) (2014) 39–45. https://doi:10.1016/j.triboint.2013.08.013.
[55] G.T.Y. Wan, H.A. Spikes, The Elastohydrodynamic Lubricating Properties of Water-Polyglycol Fire-Resistant Fluids, ASLE Trans.. 27(4) 1984 366-372. https://doi:10.1080/05698198408981582.